Retinal conduction speed analysis reveals different origins of the P50 and N95 components of the (multifocal) pattern electroretinogram

Bach M[1,2], Cuno AK[3], Hoffmann MB[3,4]

[1]University Eye Center, Medical Center – University of Freiburg, Germany

[2]Faculty of Medicine, University of Freiburg, Germany

[3]Visual Processing Laboratory, Universitäts-Augenklinik, Magdeburg, Germany

[4]Center for Behavioural Brain Sciences, Magdeburg, Germany

Corresponding author:

Prof. Michael Bach

Eye Center, Freiburg University, Killianstr. 5, 79106 Freiburg, Germany

michael.bach@uni-freiburg.de

Conflict of Interest: None of the authors have potential conflicts of interest to disclose.

Published in Experimental Eye Research 2018, 169:48–53

http://dx.doi.org/10.1016/j.exer.2018.01.021

Highlights

1. The retinal pattern electroretinogram (PERG) comprises two components, P50 and N95.
2. P50/N95 differ in functional origin and differ in their clinical significance.
3. We investigated the retinal locus of the P50 and N95 origin using multifocal stimulation (mfPERG).
4. P50/N95-like mfPERG components were found to differ in their origin; namely ganglion cell body and axons at the ONH, respectively.

Abstract

The pattern electroretinogram (PERG), an indicator of retinal ganglion cell (RGC) function, comprises a P50 and an N95 component. We addressed the question of whether the N95 originates, like the P50, from the RGC bodies or from the change of axon orientation at the optic nerve head (ONH). Thus, we recorded multifocal PERGs for 36 retinal locations in 21 participants. Second-order kernel responses were analyzed for the dependence of peak time topography on retinal fiber lengths to the ONH separately for the positive and negative excursions. We found that peak times were longer for macular [P1 (P50-like): 50 ms; N2 (N95-like): 76)] than for peripheral responses [P1: 43; N2: 66]. For the N2 another factor was necessary to explain the variability: The time difference (deltaT: N2 minus P1) was found to be proportional to fiber length from ganglion cell body to the ONH. We calculated retinal fiber length using an analytical function by Jansonius et al (2009, 2012) and found that a linear model with factors eccentricity and fiber length explained 82% of the total N2 time variance ($p<<0.001$). The conduction speeds of the retinal axons were estimated from deltaT to range from 0.5 to 3.0 m/s for parafovea and periphery, respectively. The dependence of deltaT on the distance from ganglion cell body to the ONH suggests that the N2 originates at the ONH rather than at the ganglion cell body. While the multifocal N2 peaks earlier (≈76 ms) than the non-multifocal PERG-N95 (≈95 ms), considerations of high-pass filtering and frequency dependence of the mfPERG-N2 suggest that the source separation (P50=ganglion cell body vs. N95=ONH) also holds for the non-multifocal PERG.

Keywords: retinal ganglion cells; pattern electroretinogram; conduction speed

1. Introduction

The pattern electroretinogram (PERG) is well established as a marker of retinal ganglion cell (RCG) function (Bach and Hoffmann, 2006; Maffei and Fiorentini, 1981). Consequently, it is a diagnostic aid e.g. for disorders of the optic nerves and macula (e.g., Holder, 2001) or detection of glaucoma (Bach and Hoffmann, 2008, 2006). It comprises two major components, the P50 (a positive excursion at approximately 50 ms) and the N95 (a negative excursion of more variable peak time around 95 ms in healthy subjects). These have been recognized to be differently affected by retinal pathology. There is evidence that PERG N95 originates with spiking activity of the RGCs, and that P50 largely arises in the RGCs or close by, with a contribution from non-spiking activity of the bipolar cells, resulting in post-synaptic potentials (Holder, 2001; Luo and Frishman, 2011; Viswanathan et al., 2000). Thus, the P50 likely relates to the spatial distribution and density of the underlying RGC bodies. Spiking activity occurs in the axon hillock and along the entire length of the retinal axon up to and including the optic nerve head, and N95 may therefore originate in different or multiple retinal locations. Considerations of local current flow as "seen" via the mass potential measurable at the cornea with reference to ipsilateral outer canthus (Bach et al., 2013) suggest the 90° fiber deflection at the ONH, leading to a mechanical – and consequently electrical – asymmetry as an a-priori likely source of the N95. This is also the rationale of the ONH component that can be extracted from the multifocal ERG (Sutter and Bearse, 1999).

Ophthalmological pathologies have different effects on the P50 and N95 components of the PERG (Holder, 2001). The knowledge of the origin of these two components will consequently help to identify and understand the underlying retinal pathophysiology and damage mechanisms. One way to examine the retinal location of P50 and N95 origins is the localized activation of RGCs: The multifocal pattern ERG (mfPERG) technique allows the activity of the RGCs to be compared between discrete macular areas and has been studied by a few groups (Harrison et al., 2006; Herbik et al., 2014; Hoffmann and Flechner, 2008; Klistorner et al., 2000; Langrová et al., 2007; Monteiro et al., 2012; Stiefelmeyer et al., 2004). Its low signal-to-noise ratio can be markedly improved by slow stimulation (Hoffmann and Flechner, 2008); "slow" here means that pattern change does not occur at every frame, but on e.g. every 2nd or 4th frame. We here combined slow mfPERG with a recent computational model of the retinal nerve fiber paths, aiming to investigate the retinal origins of different mfPERG components, analogous to the P50 and N95 components of the conventional transient PERG.

2. Materials and Methods

2.1. Participants

A total of 21 participants (median age: 57, range 21–78) with normal vision [visual acuity ≤0.1 logMAR] (FrACT (Bach, 2007, 1996) agreed to take part and gave their written informed consent after the nature of the experiment was explained in detail. The study design was approved by the

Ethical Committee of the University of Magdeburg, Germany and procedures were performed in accordance to the ethical standards laid down in the 1964 declaration of Helsinki (World Medical Association, 2000). The participants wore refractive correction appropriate to the testing distance, if necessary.

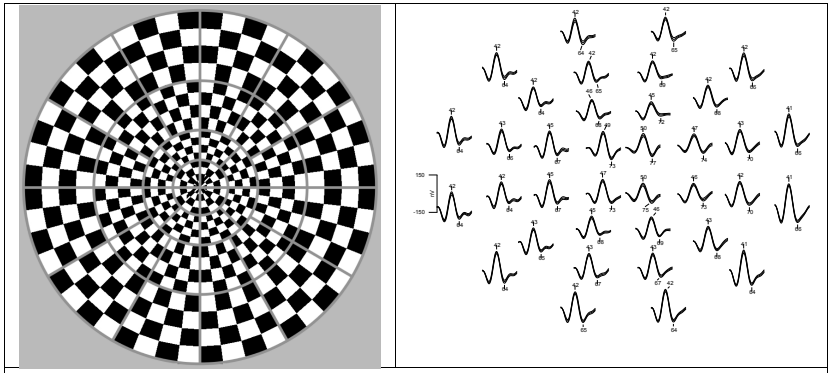

Fig. 1—Left: One stimulus phase. For each m-sequence step, a 4×4 element of the checkerboard was phase-reversed at around 18.75 reversals per second (see text). The grey lines are not visible in the actual stimulus display and added here to delineate the separate 36 contrast-reversing stimulus elements. Right: Grand mean 2nd-order kernel multifocal pattern electroretinograms from 21 normal participants depicted as if viewed through the left eye (field view) for all subjects. The SEM traces surrounding them (±SEM) are very small and consequently seem to thicken the traces. The small numbers indicate rounded peak times. A negative (N1) - positive (P1) - negative (N2) complex is clearly visible.

2.2 Stimulation and Recording

We used VERIS Science 5.1.12XScience (EDI: Electro-Diagnostic Imaging, Redwood City, CA, USA) for stimulation and recording. MfPERGs were recorded monocularly (12 left, 9 right eyes) with a DTL-electrode (Dawson et al., 1979) referenced to the ipsilateral canthus. The signal was amplified by 100 k with a physiological amplifier (Grass Model 12, Astro-Med, Inc., West Warwick, RI, USA), band-pass filtered (low and high frequency cut-offs: 3 and 300 Hz), and digitised at 1200 Hz. Stimuli were presented at a frame rate of 75 Hz. Supported by a chin rest the participants viewed the stimulus display, a circular dartboard-checkerboard pattern (mean luminance: 56 cd/m^2; contrast: 96%) covering 44° of visual angle, from a distance of 36 cm. The stimulus consisted of 36 elements which were arranged in 4 rings spanning the following eccentricity ranges: 0.0–3.6, 3.6–7.6, 7.6–14.3 and 14.3–22.7°. The central ring had 4 elements, ring 2 had 8, and ring 3 and 4 had 12 elements. Each single element comprised a 4×4 checkerboard. The 36 fields of this display were stimulated according to an m-sequence (length of 2^{14}-1), where a "1" caused reversal, a "0" left the local pattern unchanged. Fig. 1 shows at the left one frame of the multifocal stimulus, and on the right the resulting PERG traces (grand mean over the 21 participants

± SEM). Slow pattern-reversal stimulation was applied (Hoffmann and Flechner, 2008), i.e. each step lasted 2 frames (26.6 ms), resulting in an average reversal rate of 18.75 rps. This resulted in a total recording time of around 7 minutes per recording block. In total, 4 blocks were collected. Each recording block was subdivided into 32 overlapping segments, each lasting about 14 s, to allow the participants to blink and to facilitate steady fixation during the actual recording. Recording segments were occasionally contaminated by disturbances, e.g. caused by blinks, and consequently discarded online upon visual inspection and replaced by an acceptable repetition of the segment.

2.3. Analysis, PERG

Second order 1st-slice kernels were extracted using VERIS 5.01.12XScience (EDI, Inc., CA, USA) and exported for further analysis with IGOR 6.21 (WaveMetrics, Inc., OR, USA). As the polarity of the 2nd order kernels extracted with VERIS 5.01.12XScience is flipped with respect to conventional recordings (Fortune and Hood, 2003, p. 200; Sutter, 2001), the responses extracted with the 2nd order kernel were flipped back in relation to the software output for both the depiction of the traces and for the analysis. The traces for the four repetitions were averaged and digitally band-pass filtered from 3 to 35 Hz. Trace arrays recorded for the right eye were arranged to spatially correspond with left eye recordings to allow grand mean analysis of identical eccentricities. The grand mean was used for all further analyses, in Fig. 1B the grand mean traces are surrounded by ±SEMs, which are so small that they just seem to thicken the traces.

2.4. Analysis, path lengths and conduction times of retinal nerve fibers

Jansonius et al. (2012, 2009) [including the errata] published useful analytic formulas for the paths of the retinal nerve fibers. For the present problem, we implemented these formulas in R (R Development Core Team, 2014) and are making them available as "Data in Brief" (Bach and Hoffmann, submitted). We used these path morphologies to derive the fiber length leading from the respective retinal stimulation patch to the optic nerve had (Fig. 2, gray curves). A path length is calculated via the line integral; the formulas by Jansonius et al., however, cannot be analytically integrated. As an alternative, we numerically calculated the line integral using the trapezoidal rule (Wikipedia, 2017), also implemented in an R program ("Data in Brief", Bach and Hoffmann, submitted). Jansonius' formula is parameterized via the angle with which the fiber enters the ONH. This angle is defined from the center of the OHN (Fig. 2 left) in mathematical notation (90°=up). With manual iteration, we determined the angles that let fibers pass directly through the center of one of the 36 stimulation centers (yellow filled circles in Fig. 2). These are indicated as blue arcs in Fig. 2. Using these axon paths, we calculated fiber lengths (the line integrals), starting at the rim of the ONH, ending at the center of the stimulus patch. Fig. 2 (right) depicts these path lengths per location. To a first approximation, the distance from the ONH is reflected in the path length; there is a slight vertical asymmetry owing to the elevated position of the ONH. The Jansonius formula calculates fiber length in degree visual angle; to relate this to standard estimates of conduction speed, we converted from visual angle to retinal distance. For the foveal region, Drasdo and Fowler

(1974) derived 0.286 mm/°, while Hirsch and Curcio (1989) used 0.291 mm/°. We decided on a rounded value of 0.29 mm/° to calculate conduction speed here. Some stimulation centers are very close to the ONH (see Fig. 2, right), yielding near zero path length. This does not represent the large stimulus segments well, which we compensated for by setting a minimum path length of 4°.

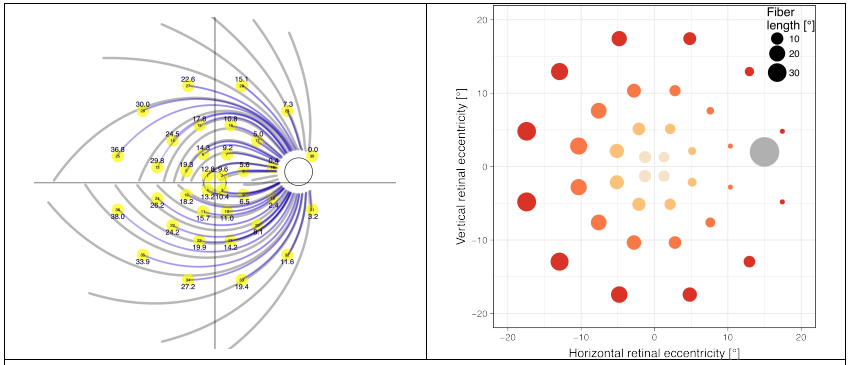

Fig. 2—Left: a schematic view of the retina, ±30° of eccentricity. Nerve fibers paths (gray) are calculated based on (Jansonius et al., 2012, 2009). Blue fibers (blue) run from the yellow numbered filled circles (indicating the centers of the stimulus patches) to the optic nerve head (open circle just above the horizontal meridian). The larger numbers represent the fiber length in degrees.

Right: In a ±20° retinal view the stimulus locations are indicated by colored filled circles (color by ring), the circle diameter encoding the particular fiber length. Length was based on the line integral from the ONH rim to the individual centers of the stimulus patches, which we calculated along the paths depicted in blue on the left. Obviously, the farther away from the ONH, the longer the path.

3. Results

3.1. Distribution of peak times

Fig. 1, right, depicts the grand mean mfPERG-trace arrays. A negative (N1)-positive (P1)-negative (N2) complex is clearly visible for each trace. These components are quite similar to the N35-P50-N95 complex of the transient human PERG (see Discussion); we will keep the more neutral NP-nomenclature for now and revisit this topic in Discussion. From the PERG traces we measured the peak times of the first negative trough (N1, N35-like, ≈ 22 ms), the major positive peak (P1, P50-like, ≈ 40–50 ms) and the second negative trough (N2, N95-like, 64–78 ms).

For the P1 component the ring-1 responses had the longest peak times (50 ms), declining to 45 ms at 10° and to 43 ms at 20° eccentricity. The subsequent negativity N2 had a somewhat similar overall topography, with longest peak times in the center (76 ms), shortening to 66 ms at 20°. In Fig. 3 these peak times are arranged by retinal location of the respective stimulus patch (left) or by

eccentricity (right). For the P1 component (top), most temporal variance (81%) can be explained by eccentricity (p<<0.001). For the N2 component (bottom), eccentricity explained 65% (p<<0.001) of variance, markedly less than for of P1. This prompts the question: Why does temporal variance across the stimulated region differ between P1 and N2?

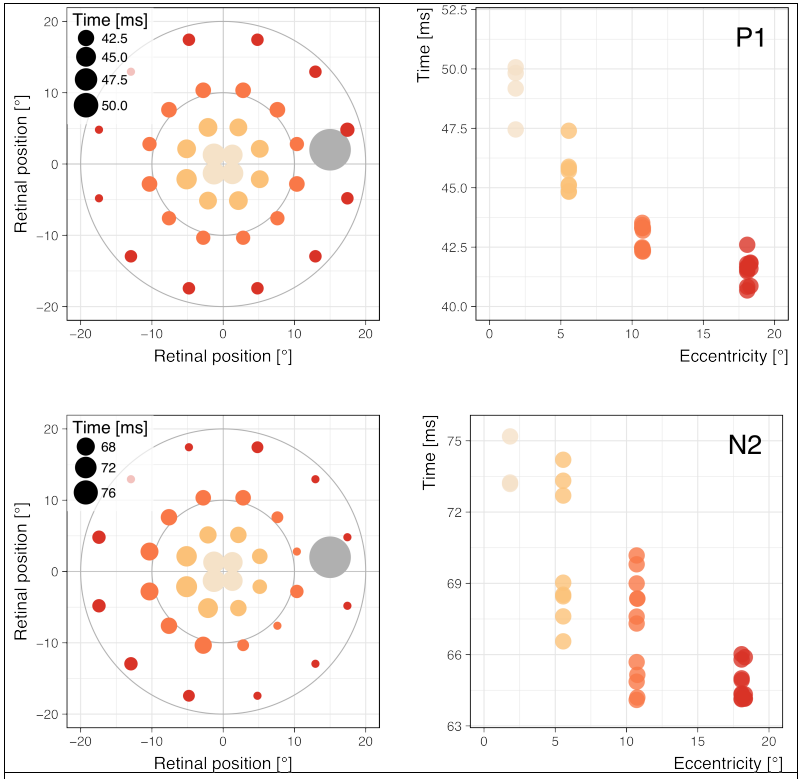

Fig. 3–Peak times of the major positive peak ("P1", top) and the second negative peak ("N2", bottom). On the left, the peak times are indicated via filled-circle size at the retinal locations, on the right the peak times (tP1 and tN2) are plotted versus retinal eccentricity (constant for each of the 4 rings). For both PERG components, the peak time significantly decreases with eccentricity (p<0.001). There is more scatter at a given eccentricity for N2 than for P1, which can mostly be attributed to fiber length (see next figure).

3.2. Fiber length per ring

Hypothesizing that the difference in temporal variance between P1 and N2 might be explained by conduction time, we analyzed the time differences $\Delta t = t_{N2} - t_{P1}$ for each retinal location tested (Fig. 4). We left out the center (ring 1), because there is too little meaningful variation across the closely adjacent four locations. An ANOVA targeting Δt with factors *eccentricity* (=ring) and *fiberlength* proved highly significant (p<<0.001) for both factors and their interaction. The interaction indicates that the slope differs significantly between rings. A linear model accounted for 82.2% of the Δt-variance with these two factors.

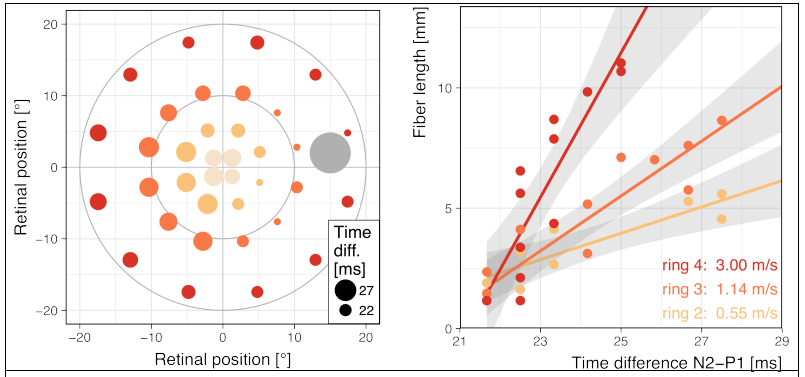

Fig. 4–Time difference of the N2 – P1 peak times, arranged by retinal position (left) or grouped by rings of constant eccentricity (right). On the left it is obvious that stimulation sites further away from the ONH have higher time differences. The chart on the right shows different slopes (≈ conduction speeds) for different eccentricities, suggesting differences in timing between N1 and P1 may be related to axon length. The lines show the linear regression; shaded areas show the standard error. Line slopes (interpreted as conduction velocities, see Discussion) are steepest for the most eccentric locations; 3.0, 1.1 and 0.55 m/s for rings 4, 3 and 2 respectively.

4. Discussion

We analyzed how peak times of the P1 and N2 components in the mfPERG depend on retinal location with the goal to better understand the physical location of the source of these components. P1 timing was relatively constant within a ring (constant eccentricity), but increased from 20° towards the center by nearly 10 ms (Fig. 3, top). Recent findings by Sinha et al. (2017) suggest that this eccentricity dependence is due to the long cone axons in the center. The N2 timing, in addition to a strong eccentricity dependence, varies also along a ring (Fig. 3, bottom). By calculating the N2-P1 time difference, two variance sources were found to explain most to the N2 peak time variation: on the one hand eccentricity, like for the P1, on the other hand the length of the retinal nerve fibers from the ganglion cell body to the ONH, as evident from Fig. 4, right.

4.1. What does the mfPERG time topography suggest for the source location of N2?

We start with the assumption that the electrical source of the P1 is the RGC body and any pre-ganglionic regions close by. For the N2, the systematic variation of the response timing suggests that the electrical field is not generated within the ganglion cell body, but rather from some area along the fiber. In particular, the kink at their entry into the ONH is a likely source. One way to gain information on this aspect is to calculate conduction speed from time difference and fiber length. This conduction speed was estimated via the slope of the regression line that relates fiber length and N2–P1 time difference, resulting in the following conduction velocities: ring 2, 0.55 m/s; ring 3, 1.14 m/s; ring 4, 3.0 m/s (Fig. 4, right). These speeds closely correspond to those obtained via the mfERG-derived optic nerve head response, see Fig. 5; (Shimada et al., 2005; Sutter and Bearse, 1999). This suggests that the N2 stems largely from axon entry into the ONH.

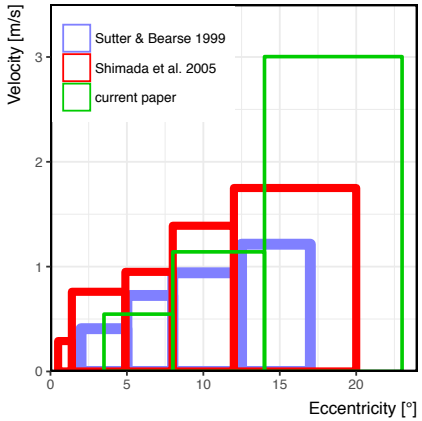

Fig. 5–Comparison of retinal fiber conduction speeds vs. eccentricity estimated in three studies (see inset). Each study covered different eccentricities in three to five rings and gave an estimate average over an eccentricity range.

There is good agreement between all three studies, except for the highest eccentricity with higher estimates in the present study.

4.2. How do mfPERG P1 and N1 source locations relate to transient PERG P50 and N95?

Previous studies investigating patients with optic nerve atrophy induced by chiasmal compression reported a correlation of retinal nerve fiber thickness measures from SD-OCT with mfPERG amplitudes (Monteiro et al., 2013, 2012) and consequently suggest that the mfPERG, like the PERG (Bach et al., 1992a; Bach and Hoffmann, 2006, 2008; Harrison et al., 1987), reflects the function of RGCs and their axons. This analogy of the mfPERG and PERG components is also supported by the similar trace shapes of the PERG and the mfPERG recorded in the present study (Fig. 1, right), which indicate the N35-P50-N95, typical of the PERG, also to be reflected in the mfPERG N1-P1-N2 complex. [It should be noted that the standard Sutter algorithm to extract the 2nd order kernel

(Sutter, 2000) leads to polarity-inverted traces which we flipped here, to comply with the transient PERG polarity convention. This procedure varies between studies and is sometimes only available through personal communication with the authors.] It must be noted though, that the peak times of the mfPERG-N2 (64–75 ms) are always below 95 ms of the eponymous PERG-N95. We can understand this apparent discrepancy by examining methodological distinctions between mfPERGS and transient PERGs, i.e. the different temporal stimulation rate applied in both recording approaches. For the conventional PERG with its well-defined P50/N95 components the temporal stimulation rate should be ≤4 rps (corresponding to ≤2 Hz). For the mfPERG, stimulation rate is frequently given in terms of “frames”, which refers to the minimum duration of a specific contrast polarity and hence determines the maximum rate of stimulation, i.e. pattern reversal. Typically, a frame lasts 13.3 ms, hence leading to a maximal stimulation rate of 75 rps, and an average stimulation rate (for a 50% chance to change contrast polarity) of 37.5 rps. For the mfPERG the duration ranges from 1 frame (Harrison et al., 2006) over 2 frames (e.g., Klistorner et al. 2000; Herbik et al. 2014) to 8 (Hoffmann and Flechner, 2008) and even slower (Monteiro et al., 2012). Hoffmann and Flechner (2008) employed 1, 2, 4, and 8 frames, allowing for the assessment of wave shape changes vs. stimulation rate. It turns out that at 1 frame, the N2 is very small, and N2 only becomes well identifiable at 2 frames and more. This is in keeping with the traces presented by Harrison et al. (2006), where the N2 is hardly recognizable for both human and non-human primates. Importantly, the comparison from 1 to 8 frames reveals that the peak time becomes progressively shorter for higher stimulation rates, bordering 95 ms for 4 and 8 frames (Fig. 5 in Hoffmann and Flechner 2008). In the present study 2 frames were employed, so an N95-like N2 was expected, but at a lower peak time as for the conventional PERG-N95.

A further shortening of the peak time is caused by high-pass filtering. The ISCEV PERG Standard (Bach et al., 2013) suggests high-pass filtering at a cut-off frequency of 1 Hz. For multifocal recording a higher value is advantageous, we used the lower limit (3 Hz) suggested in the mfERG Standard (Hood et al., 2012). To assess filtering effects on our traces, we filtered the original 2013-PERG standard trace with a simulated first-order high-pass filter at 3 Hz (Abächerli et al., 2016), and found that the N95 peak time reduced by 5 ms from 96 ms to 91 ms (P50 only by 1 ms, from 48 ms to 47 ms). Combined with the peak-time changes due to the rapid stimulation discussed above, the peak time of N2 would be in the range of the N95. All-in-all, we conclude that the present mfPERG-N2 and the standard PERG-N95 represent the same component.

4.3. Consequences for future studies

Given the different origin of the P50-like P1 and N95-like N2 of the mfPERG – and hence the P50 and N95 of the conventional PERG – a differential analysis of these components appears to bear potential for patient investigations, e.g. via the identification of the site of retinal/postretinal damage. Optimal differentiation of P1 and N1 components is enabled by relatively slow rate of stimulation, namely change every 2 frames or slower, as suggested by Harrison et al. (2006) and Hoffmann & Flechner (2008), optimizing the signal to noise ratio and enhancing the N2 component.

As the mfPERG method has not been standardized, it is important that future studies involving this technique, fully specify the stimulation and analysis parameters to enable appropriate interpretation of the data.

5. Conclusions

The timing of mfPERG P1 is highly dependent on retinal eccentricity (probably due to cone timing). The additional timing variance of the N1 is explained by the finding that the time difference between P1 and N2 is proportional to the fiber length between the retinal ganglion cell bodies and the optic nerve head. Analysis of conduction velocity suggests that the N2 is generated at the optic nerve head. Considerations of stimulation rate and filtering suggest that mfPERG's P1 corresponds to PERG's P50, and mfPERG's N2 to PERG's N95 in spite of the earlier peak times in the mfPERG. Our findings confirm that the P50 and N95 components in the widely used transient pattern ERG have important differences in origin that may be useful for clinical and diagnostic purposes.

Acknowledgement

We thank Lea Atala-Gérard for help in assessing the analytical integration problem of the Jansonius formula. Two anonymous reviewers went to great length with helpful suggestions to improve the manuscript.

References

Abächerli, R., Isaksen, J., Schmid, R., Leber, R., Schmid, H.-J., Generali, G., 2016. Digital DC-Reconstruction of AC-Coupled Electrophysiological Signals with a Single Inverting Filter. PLoS ONE 11, e0150207. https://doi.org/10.1371/journal.pone.0150207

Bach, M., 2007. The Freiburg Visual Acuity Test – Variability unchanged by post-hoc re-analysis. Graefes Arch Clin Exp Ophthalmol 245, 965–71.

Bach, M., 1996. The Freiburg Visual Acuity Test – Automatic measurement of visual acuity. Optom Vis Sci 73, 49–53.

Bach, M., Brigell, M.G., Hawlina, M., Holder, G.E., Johnson, M.A., McCulloch, D.L., Meigen, T., Viswanathan, S., 2013. ISCEV standard for clinical pattern electroretinography (PERG): 2012 update. Doc Ophthalmol 124, 1–13. https://doi.org/10.1007/s10633-012-9353-y

Bach, M., Gerling, J., Geiger, K., 1992. Optic atrophy reduces the pattern-electroretinogram for both fine and coarse stimulus patterns. Clin Vision Sci 7, 327–333.

Bach, M., Hoffmann, M.B., 2008. Update on the pattern electroretinogram in glaucoma. Optom Vis Sci 85, 386–95.

Bach, M., Hoffmann, M.B., 2006. The Origin of the Pattern Electroretinogram (PERG), in: Heckenlively, J., Arden, G. (Eds.), Principles and Practice of Clinical Electrophysiology of Vision. MIT Press, Cambridge, London, pp. 185–196.

Bach, M., Hoffmann, M.B., submitted. An R program to calculate and plot retinal nerve fibers based on Jansonius et al. 2009/2012. Data in Brief.

Dawson, W.W., Trick, G.L., Litzkow, C.A., 1979. Improved electrode for electroretinography. Invest Ophthalmol Vis Sci 18, 988–91.

Drasdo, N., Fowler, C.W., 1974. Non-linear projection of the retinal image in a wide-angle schematic eye. Br J Ophthalmol 58, 709–714.

Fortune, B., Hood, D.C., 2003. Conventional pattern-reversal VEPs are not equivalent to summed multifocal VEPs. Investigative Ophthalmology & Visual Science 44, 1364–75.

Harrison, J.M., O'Connor, P.S., Young, R.S.L., Kincaid, M., Bentley, R., 1987. The pattern ERG in man following surgical resection of the optic nerve. Invest Ophthalmol Vis Sci 28, 492–499.

Harrison, W.W., Viswanathan, S., Malinovsky, V.E., 2006. Multifocal pattern electroretinogram: cellular origins and clinical implications. Optom Vis Sci 83, 473–85.

Herbik, A., Reupsch, J., Thieme, H., Hoffmann, M.B., 2014. Differential effects of optic media opacities on simultaneous multifocal pattern electroretinograms and visual evoked potentials. Clinical Neurophysiology 125, 2418–2426. https://doi.org/10.1016/j.clinph.2014.03.017

Hirsch, J., Curcio, C.A., 1989. The spatial resolution capacity of human foveal retina. Vision Research 29, 1095–1101. https://doi.org/10.1016/0042-6989(89)90058-8

Hoffmann, M.B., Flechner, J.-J., 2008. Slow pattern-reversal stimulation facilitates the assessment of retinal function with multifocal recordings. Clin Neurophysiol 119, 409–417. https://doi.org/10.1016/j.clinph.2007.10.005

Holder, G.E., 2001. Pattern electroretinography (PERG) and an integrated approach to visual pathway diagnosis. Prog Retin Eye Res 20, 531–61.

Hood, D.C., Bach, M., Brigell, M., Keating, D., Kondo, M., Lyons, J.S., Marmor, M.F., McCulloch, D.L., Palmowski-Wolfe, A.M., 2012. ISCEV standard for clinical multifocal electroretinography (mfERG) (2011 edition). Documenta Ophthalmologica. Advances in Ophthalmology 124, 1–13. https://doi.org/10.1007/s10633-011-9296-8

Jansonius, N.M., Nevalainen, J., Selig, B., Zangwill, L.M., Sample, P.A., Budde, W.M., Jonas, J.B., Lagrèze, W.A., Airaksinen, P.J., Vonthein, R., Levin, L.A., Paetzold, J., Schiefer, U., 2009. A mathematical description of nerve fiber bundle trajectories and their variability in the human retina. Vision Res. 49, 2157–2163. https://doi.org/10.1016/j.visres.2009.04.029

Jansonius, N.M., Schiefer, J., Nevalainen, J., Paetzold, J., Schiefer, U., 2012. A mathematical model for describing the retinal nerve fiber bundle trajectories in the human eye: average course, variability, and influence of refraction, optic disc size and optic disc position. Exp. Eye Res. 105, 70–78. https://doi.org/10.1016/j.exer.2012.10.008

Klistorner, A.I., Graham, S.L., Martins, A., 2000. Multifocal pattern electroretinogram does not demonstrate localised field defects in glaucoma. Doc Ophthalmol 100, 155–165.

Langrová, H., JäGle, H., Zrenner, E., Kurtenbach, A., 2007. The multifocal pattern electroretinogram (mfPERG) and cone-isolating stimuli. Visual Neuroscience 24, 805–816. https://doi.org/10.1017/S0952523807070733

Luo, X., Frishman, L.J., 2011. Retinal pathway origins of the pattern electroretinogram (PERG). Invest Ophthalmol Vis Sci 52, 8571–8584. https://doi.org/10.1167/iovs.11-8376

Maffei, L., Fiorentini, A., 1981. Electroretinographic responses to alternating gratings before and after section of the optic nerve. Science 211, 953–954.

Monteiro, M.L.R., Hokazono, K., Cunha, L.P., Oyamada, M.K., 2013. Correlation between multifocal pattern electroretinography and Fourier-domain OCT in eyes with temporal hemianopia from chiasmal compression. Graefe's Archive for Clinical and Experimental Ophthalmology 251, 903–915. https://doi.org/10.1007/s00417-012-2156-8

Monteiro, M.L.R., Hokazono, K., Cunha, L.P., Oyamada, M.K., 2012. Multifocal pattern electroretinography for the detection of neural loss in eyes with permanent temporal hemianopia or quadrantanopia from chiasmal compression. British Journal of Ophthalmology 96, 104–109. https://doi.org/10.1136/bjo.2010.199661

R Development Core Team, 2014. R: A Language and Environment for Statistical Computing [WWW Document]. URL http://www.R-project.org (accessed 8.18.14).

Shimada, Y., Horiguchi, M., Nakamura, A., 2005. Spatial and temporal properties of interocular timing differences in multifocal visual evoked potentials. Vision Research 45, 365–371. https://doi.org/10.1016/j.visres.2004.08.016

Sinha, R., Hoon, M., Baudin, J., Okawa, H., Wong, R.O.L., Rieke, F., 2017. Cellular and Circuit Mechanisms Shaping the Perceptual Properties of the Primate Fovea. Cell 168, 413–426.e12. https://doi.org/10.1016/j.cell.2017.01.005

Stiefelmeyer, S., Neubauer, A.S., Berninger, T., Arden, G.B., Rudolph, G., 2004. The multifocal pattern electroretinogram in glaucoma. Vision Res 44, 103–12.

Sutter, E.E., 2001. Imaging visual function with the multifocal m-sequence technique. Vision Research 41, 1241–55.

Sutter, E.E., 2000. The interpretation of multifocal binary kernels. Doc Ophthalmol 100, 49–75.

Sutter, E.E., Bearse, M.A., 1999. The optic nerve head component of the human ERG. Vision Research 39, 419–436.

Viswanathan, S., Frishman, L.J., Robson, J.G., 2000. The uniform field and pattern ERG in macaques with experimental glaucoma: removal of spiking activity. Invest Ophthalmol Vis Sci 41, 2797–810.

Wikipedia, 2017. Trapezoidal rule [WWW Document]. Trapezoidal rule. URL https://en.wikipedia.org/w/index.php?title=Trapezoidal_rule&oldid=816212620 (accessed 12.31.17).

World Medical Association, 2000. Declaration of Helsinki: ethical principles for medical research involving human subjects. J Am Med Assoc 284, 3043–3045.